

Tropical Precipitation and Cross-Equatorial Ocean Heat Transport during the Mid-Holocene

XIAOJUAN LIU AND DAVID S. BATTISTI

Department of Atmospheric Sciences, University of Washington, Seattle, Washington

AARON DONOHOE

Applied Physics Laboratory, University of Washington, Seattle, Washington

(Manuscript received 14 July 2016, in final form 3 January 2017)

ABSTRACT

Summertime insolation intensified in the Northern Hemisphere during the mid-Holocene, resulting in enhanced monsoonal precipitation. In this study, the authors examine the changes in the annual-mean tropical precipitation as well as changes in atmospheric circulation and upper-ocean circulation in the mid-Holocene compared to the preindustrial climate, as simulated by 12 coupled climate models from PMIP3. In addition to the predominant zonally asymmetric changes in tropical precipitation, there is a small northward shift in the location of intense zonal-mean precipitation (mean ITCZ) in the mid-Holocene in the majority (9 out of 12) of the coupled climate models. In contrast, the shift is southward in simulations using an atmospheric model coupled to a slab ocean. The northward mean ITCZ shift in the coupled simulations is due to enhanced northward ocean heat transport across the equator [OHT(EQ)], which demands a compensating southward atmospheric energy transport across the equator, accomplished by shifting the Hadley cell and hence the mean ITCZ northward. The increased northward OHT(EQ) is primarily accomplished by changes in the upper-ocean gyre circulation in the tropical Pacific acting on the zonally asymmetric climatological temperature distribution. The gyre intensification results from the intensification of the monsoonal winds in the Northern Hemisphere and the weakening of the winds in the Southern Hemisphere, both of which are forced directly by the insolation changes.

1. Introduction

By the time of the mid-Holocene, roughly 6000 yr ago, the large continental ice shelves that occupied much of North America during the last glaciation had retreated to near-modern-day extent (Paillard 2010), and greenhouse gas concentrations were also near-modern-day values. Hence, the main driver of climatic differences between the mid-Holocene and present day was differences in Earth's orbit about the sun: (i) Earth's elliptical orbit about the sun passed closest to the sun in late August during the mid-Holocene compared to early January in the present-day orbital configuration, resulting in more (less) intense insolation during boreal (austral) summer (Fig. 4 of Bosmans et al. 2012); and (ii) the obliquity was slightly higher during the mid-Holocene, resulting in greater high-latitude (less

tropical) insolation compared to modern day. There is ample geological and geochemical evidence that the changes in insolation at the mid-Holocene modulate the climate, especially precipitation in the tropics. The fossil pollen and lake sediments from Africa show that the Sahel and Sahara regions were considerably wetter during the mid-Holocene than at present (Street and Grove 1976; Jolly et al. 1998; Bartlein et al. 2011). The sediment record from the Cariaco Basin suggests that precipitation over the northern tip of South America was enhanced during the mid-Holocene (Haug et al. 2001). Similarly, oxygen isotope records in speleothems around the Indian Ocean basin are consistent with a more intense Indian monsoon in the mid-Holocene than at present (LeGrande and Schmidt 2009). Whether the compilation of these records suggests an intensification of the Northern Hemisphere summer monsoon systems (Boos and Korty 2016) or a more zonally homogenous northward shift/expansion of the

Corresponding author e-mail: Xiaojuan Liu, xjliu@uw.edu

DOI: 10.1175/JCLI-D-16-0502.1

© 2017 American Meteorological Society. For information regarding reuse of this content and general copyright information, consult the [AMS Copyright Policy](http://www.ametsoc.org/PUBSReuseLicenses) (www.ametsoc.org/PUBSReuseLicenses).

tropical precipitation (Collins et al. 2011a; Arbuszewski et al. 2013) is subject to interpretation.

Numerical modeling studies show that the precipitation response to mid-Holocene orbital changes is zonally asymmetric and seasonally heterogeneous. There is a robust enhancement of the Northern Hemisphere summer monsoon and a weakening of the Southern Hemisphere summer monsoon (Kutzbach and Guetter 1986; Joussaume et al. 1999; Braconnot et al. 2007a; Prado et al. 2013; Battisti et al. 2014; Liu and Battisti 2015). Braconnot et al. (2007b) show that intense tropical precipitation extended farther north during the boreal summer over India, the Sahel, and western Africa—with much smaller changes over the ocean (see their Fig. 3b)—in all the mid-Holocene simulations participating in the phase 2 of the Paleoclimate Modeling Intercomparison Project (PMIP2). This zonal asymmetry in the precipitation response to mid-Holocene orbital changes is common to almost all simulations of the mid-Holocene no matter whether a slab or a dynamic ocean is used (cf. Figs. 1a and 1b; see also Hsu et al. 2010; K. Chamales et al. 2017, manuscript submitted to *Geophys. Res. Lett.*). It is also present in experiments with more extreme precessional forcing, such as the difference between 11 kyr BP and modern day and the difference between 218 and 207 kyr BP (Clement et al. 2004; Battisti et al. 2014; Liu and Battisti 2015). By synthesizing the paleoclimate records and results from climate model simulations of the mid-Holocene, McGee et al. (2014) argue that zonal-mean precipitation changes were remarkably small (ITCZ shifts could not have exceeded 50 km) and the precipitation changes inferred from mid-Holocene proxy records are primarily regionally and seasonally heterogeneous.

Despite the predominant zonally and seasonally inhomogeneous characteristic of tropical precipitation changes during the mid-Holocene, we demonstrate here that coupled model simulations of the mid-Holocene have a robust northward shift of the annual-mean, zonal-mean tropical precipitation (called mean ITCZ in the following text for convenience). The majority (9 out of 12) of the phase 3 of the Paleoclimate Modeling Intercomparison Project (PMIP3) models shift the mean ITCZ northward in response to mid-Holocene orbital parameters (see Fig. A2 in the appendix). This is consistent with the findings of Donohoe et al. (2013), who documented a robust northward mean ITCZ shift in the previous generation (PMIP2) of coupled climate model simulations of the mid-Holocene. A northward ITCZ shift requires anomalous energy input to the atmosphere in the Northern Hemisphere and atmospheric cooling in the Southern Hemisphere [see review by Schneider et al. (2014)].

Therefore, the robust northward ITCZ shift in the mid-Holocene seen in the climate models (each of which has a unique physical package) suggests a basic underlying mechanism for the hemispherical asymmetric energy input to the Northern Hemisphere atmosphere due to changes in either radiative processes or ocean dynamics.

While the mean ITCZ shifts northward in the PMIP3 models that feature an atmospheric general circulation model coupled to a dynamic ocean model, it shifts southward when an atmospheric general circulation model is coupled to a slab ocean model. This includes the ECHAM4.6 used in this study (Battisti et al. 2014; Liu and Battisti 2015) and the CCSM3 (K. Chamales 2013, personal communication). That the sign of the meridional displacement of mean ITCZ depends on whether the models employ a dynamic ocean provides a fortuitous window for understanding how changes in ocean circulation in response to precessional forcing impact the tropical precipitation.

This paper studies the tropical, zonal-mean, annual-mean precipitation change in PMIP3 simulations of the mid-Holocene. We take as a starting point that the fundamental precipitation and circulation response to mid-Holocene orbital forcing is the enhancement of the Northern Hemisphere summer monsoon, which has been noted extensively in the literature, and that this response is the direct response to the insolation change, which does not depend on dynamical coupling to an ocean. We emphasize that while the mid-Holocene precipitation changes are dominated by this seasonally and zonally inhomogeneous response, the focus of this manuscript is how the hemispherically asymmetric changes in monsoon strength impact the zonal-mean ITCZ location. We invoke the following mechanism to explain the northward ITCZ shift in coupled climate models and the near-zero ITCZ shift in models without a dynamic ocean (see Fig. 5, below): (i) the wind stress change due to the enhanced Northern Hemisphere (diminished Southern Hemisphere) summer monsoon increases the circulation of the northern tropical Pacific Ocean Gyre (decreases the circulation of the southern tropical Pacific Gyre), bringing energy into the Northern Hemisphere; and (ii) the Northern Hemisphere atmosphere is heated, resulting in a northward mean ITCZ shift. The latter process can be thought of as resulting from the compensating cross-equatorial energy transport between the ocean and the atmosphere whereby the enhanced northward ocean energy transport across the equator is (partially) balanced by a compensating southward atmospheric energy transport across the equator associated with a northward-shifted Hadley cell and

TABLE 1. List of the model names, resolutions, and references for the PMIP3 models used in this study. Also shown is the length of the preindustrial (PI) and the mid-Holocene (6K) simulations. When there was an ensemble of runs for an experiment, climatologies were calculated using the first ensemble member. (Expansions of acronyms are available online at <http://www.ametsoc.org/PubsAcronymList>.)

Model name	Institution	Resolution		Reference	Length of run (yr)	
		Atmospheric (lat × lon or spectral, vertical levels)	Oceanic (lat × lon grid points, vertical levels)		PI	6K
BCC_CSM1.1	Beijing Climate Center, China Meteorological Administration, China	T42, L26	232 × 360, L40	Xin et al. (2013)	500	100
CCSM4	National Center for Atmospheric Research, United States	0.9° × 1.25°, L26	384 × 320, L60	Gent et al. (2011)	1050	300
CNRM-CM5	Center National de Recherches Météorologiques, France	T127, L31	292 × 362, L42	Voldoire et al. (2013)	850	200
CSIRO Mk3.6.0	Commonwealth Scientific and Industrial Research Organisation in collaboration with the Queensland Climate Change Centre of Excellence, Australia	T63, L18	189 × 192, L31	Rotstayn et al. (2010)	500	100
CSIRO Mk3L1.2	University of New South Wales, Sydney, Australia	R21, L18	122 × 128, L21	Phipps et al. (2011)	1000	500
FGOALS-g2	LASG, Institute of Atmospheric Physics, Chinese Academy of Sciences; and Center for Earth System Science, Tsinghua University, China	2.81° × 2.81°, L26	196 × 360, L30	Li et al. (2013)	700	685
FGOALS-s2	LASG, Institute of Atmospheric Physics, Chinese Academy of Sciences, China	T42, L26	196 × 360, L30	Bao et al. (2013)	500	100
GISS-E2-R	NASA Goddard Institute for Space Studies, United States	2° × 2.5°, L20	180 × 288, L32	Schmidt et al. (2006)	1200	100
MIROC-ESM	Japan Agency for Marine-Earth Science and Technology, Atmosphere and Ocean Research Institute (The University of Tokyo), and National Institute for Environmental Studies, Japan	T42, L80	192 × 256, L44	Watanabe et al. (2011)	630	100
MRI-CGCM3	Meteorological Research Institute, Japan	T159, L48	368 × 360, L51	Yukimoto et al. (2012)	500	100
HadGEM2-ES	Met Office Hadley Centre, United Kingdom	1.875° × 1.25°, L38	—	Collins et al. (2011b) ; Jones et al. (2011) ; Martin et al. (2011)	577	100
MPI-ESM-P	Max Planck Institute for Meteorology, Germany	T63, L47	220 × 256, L40	Raddatz et al. (2007) ; Marsland et al. (2003)	1155	100

mean ITCZ ([Frierson et al. 2013](#)). We expand on and elaborate on the mechanisms modulating the mean ITCZ and the central role of changes in the ocean circulation in this manuscript.

2. Data and methods

a. Model runs used

We make use of the output from PMIP3, wherein the climates of preindustrial and mid-Holocene were simulated using climate models that include the full dynamic

ocean module ([Braconnot et al. 2012](#)). We analyzed all models for which the requisite output required for the analyses we perform is publicly available; details of the models and references are found in [Table 1](#). The major difference between the preindustrial and the mid-Holocene simulations is insolation: in the mid-Holocene, perihelion is in boreal summer (around 21 August),¹ and there is a slightly greater obliquity than today; perihelion in

¹ Vernal equinox is fixed on 21 March.

the preindustrial and modern climate is in boreal winter (around 3 January). This leads to an increase of insolation by 21 W m^{-2} at 20°N in the Northern Hemisphere summer (June–August) and to a decrease of insolation in the Southern Hemisphere summer [December–February; see Fig. 4 of [Bosmans et al. \(2012\)](#)] during the mid-Holocene compared to today. The change in mean ITCZ is therefore due to both change in precession and change in obliquity, with a dominant contribution from the change in precession.

Each simulation used the same boundary conditions for the mid-Holocene and preindustrial simulations: ice sheet geometry, topography, and greenhouse gas concentrations, except for CH_4 concentration, which is reduced from 760 ppb in the preindustrial simulation to 650 ppb in the mid-Holocene simulation ([Taylor et al. 2012](#); <https://pmip3.lsce.ipsl.fr>). The resulting difference in radiative forcing due to changes in CH_4 is negligible compared to the orbitally induced changes in insolation. We use the monthly climatological data downloaded from the CMIP5 data portal (http://cmip-pcmdi.llnl.gov/cmip5/data_portal.html).

b. Energetic analysis

The position of mean ITCZ is closely linked to the cross-equatorial energy transport by the atmosphere, with a northward displacement of the mean ITCZ corresponding to a southward atmospheric energy transport across the equator because the meridional transport of moisture, sensible heat, and potential energy in the deep tropics is primarily accomplished by the Hadley circulation. Thus, understanding changes in the position of mean ITCZ is synonymous with understanding the changes in interhemispheric energy transport and the energetic processes that lead to such changes. In equilibrium, divergence of the atmospheric energy transport $\nabla \cdot \text{AHT}$ is balanced by the net input energy to the atmosphere F_{net} :

$$\nabla \cdot \text{AHT} = F_{\text{TOA}} + F_{\text{SFC}} \equiv F_{\text{net}}, \quad (1)$$

where F_{TOA} is the net radiation at the top of the atmosphere, and F_{SFC} is the net heat flux entering the atmosphere from the surface. The northward atmospheric energy transport across a latitude band $\text{AHT}(\phi)$ can then be calculated by integrating Eq. (1) as follows:

$$\text{AHT}(\phi) = R^2 \int_{-\pi/2}^{\phi} \int_0^{2\pi} F_{\text{net}} \cos\phi \, d\lambda \, d\phi, \quad (2)$$

where R is the radius of Earth, and $F_{\text{net}} = F_{\text{TOA}} + F_{\text{SFC}}$ is a function of latitude ϕ and longitude λ . The cross-equatorial atmospheric energy transport $\text{AHT}(\text{EQ}) \equiv$

$\text{AHT}(\phi = 0)$ can be expressed as either the integral of the net energy into the atmosphere from the South Pole to the equator or from the equator to the North Pole as follows:

$$\text{AHT}(\text{EQ}) = R^2 \int_{-\pi/2}^0 \int_0^{2\pi} F_{\text{net}} \cos\phi \, d\lambda \, d\phi \quad \text{and} \quad (3)$$

$$= -R^2 \int_0^{\pi/2} \int_0^{2\pi} F_{\text{net}} \cos\phi \, d\lambda \, d\phi, \quad (4)$$

which can also be written as

$$\begin{aligned} \text{AHT}(\text{EQ}) &= -\frac{1}{2}([F_{\text{net}}]_{\text{SH}}^{\text{NH}}) \\ &= -\frac{1}{2}([F_{\text{TOA}} + F_{\text{SFC}}]_{\text{SH}}^{\text{NH}}), \end{aligned} \quad (5)$$

where the square brackets denote the integral over the hemisphere. Equation (5) states that the hemispheric asymmetry in net energy into the atmosphere is balanced by atmospheric energy transport across the equator from the hemisphere receiving excess energy to the hemisphere with a net energy loss. The $\text{AHT}(\text{EQ})$ is equal to the asymmetry in hemispherically integrated F_{net} , which, in turn, is due to the hemispheric asymmetry in F_{TOA} , F_{SFC} , or both.

3. Results

a. Changes in precipitation at the mid-Holocene

[Figure 1a](#) shows the multimodel-mean change (hereinafter we define change as mid-Holocene minus preindustrial) in the precipitation between the mid-Holocene and the preindustrial simulations from the PMIP3 models. [Figure 1b](#) shows the same change but from the ECHAM4.6 model coupled to a 50-m slab ocean. The dominant features in the model with the slab ocean and in the models with a dynamic ocean are the shifts in precipitation from the ocean to the land in the Northern Hemisphere and from the land to the ocean in the Southern Hemisphere. This land–sea asymmetry is also seen in other modeling studies ([Kutzbach and Guetter 1986](#); [Clement et al. 2004](#); [Braconnot et al. 2007a](#); [Hsu et al. 2010](#)), including those associated with stronger precessional cycles ([Bartlein et al. 2011](#); [Battisti et al. 2014](#); [Liu and Battisti 2015](#)); the stronger Northern Hemisphere summer insolation in the mid-Holocene shifts the location of the maximum moist entropy from the Bay of Bengal and Southeast Asia to be over northern India and the Arabian Peninsula ([Battisti et al. 2014](#)). Similarly, the reduced summer (December–February)

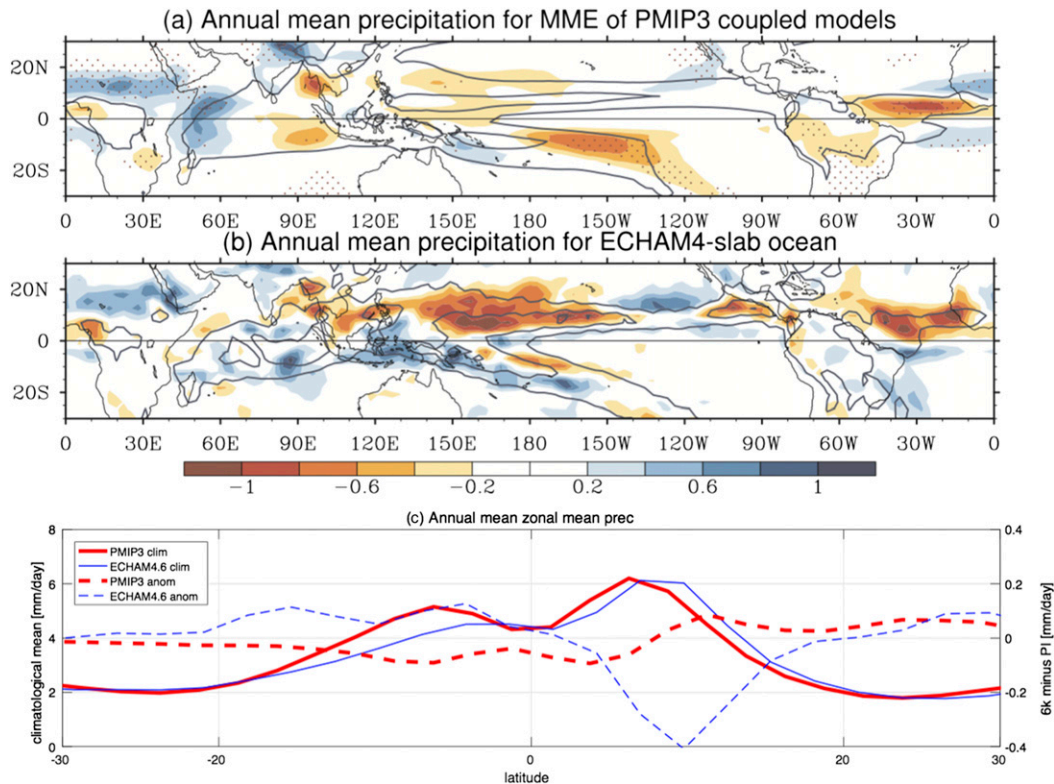


FIG. 1. (a) The multimodel mean of climatological annual-mean precipitation in the preindustrial experiment (contours; mm day^{-1}), and of the change in precipitation (mid-Holocene minus preindustrial) from the PMIP3 models (shaded; mm day^{-1}). All of the PMIP3 climate models include dynamic oceans. (b) As in (a), but for ECHAM4.6-slab ocean model. (c) Zonal-mean, annual-mean, climatological precipitation (solid lines; mm day^{-1}) and change in precipitation (dashed lines; mm day^{-1}) from the PMIP3 models (red) and from the ECHAM4.6-slab ocean model (blue).

insolation over South America and southern Africa in the mid-Holocene reduces moist entropy and thus precipitation in these regions compared to that over the adjacent oceans (Liu and Battisti 2015). Note that change in the multimodel-mean precipitation in the PMIP3 models is not as strong as that in the ECHAM4.6-slab ocean model because averaging over all models partly smooths out the signal and—unlike the circulation changes (see section 3c)—details in spatial pattern of the precipitation change can differ substantially from the multimodel mean in some models.

It is worth mentioning that the change in precipitation in the mid-Holocene compared to preindustrial also features a northward shift of ITCZ over the land in the boreal summer and a southward shift of ITCZ over the ocean in austral summer [not shown; please refer to Braconnot et al. (2007b) for more details]. This might be related to the slight increase in obliquity, which enhances the summer insolation and weakens the winter insolation in both hemispheres equally. Nonetheless, its

contribution to the mean ITCZ shift is negligible (Mantsis et al. 2011).

The change in the annual-mean, zonal-mean precipitation in models that include a dynamic ocean is shown in Fig. 1c (red dashed line). In the mid-Holocene, there is an increase in precipitation north of the mean rainfall peak in the preindustrial and a decrease in precipitation south of it, indicating a northward shift of the mean ITCZ (Fig. 1c). Contrary to the results from the PMIP3 models that have dynamic oceans, the mean ITCZ shifts southward in the mid-Holocene compared to the preindustrial simulation using the ECHAM4.6 model, which is coupled to a slab ocean. A southward shift in the mean ITCZ is also seen in the extreme precession experiments using the ECHAM4.6 model coupled to a slab ocean (Battisti et al. 2014; Liu and Battisti 2015) and in a pair of summer perihelion versus winter perihelion experiments using CCSM3 coupled to a slab ocean (K. Chamales 2013, personal communication). That ocean dynamics is responsible for the difference in the directions of mean

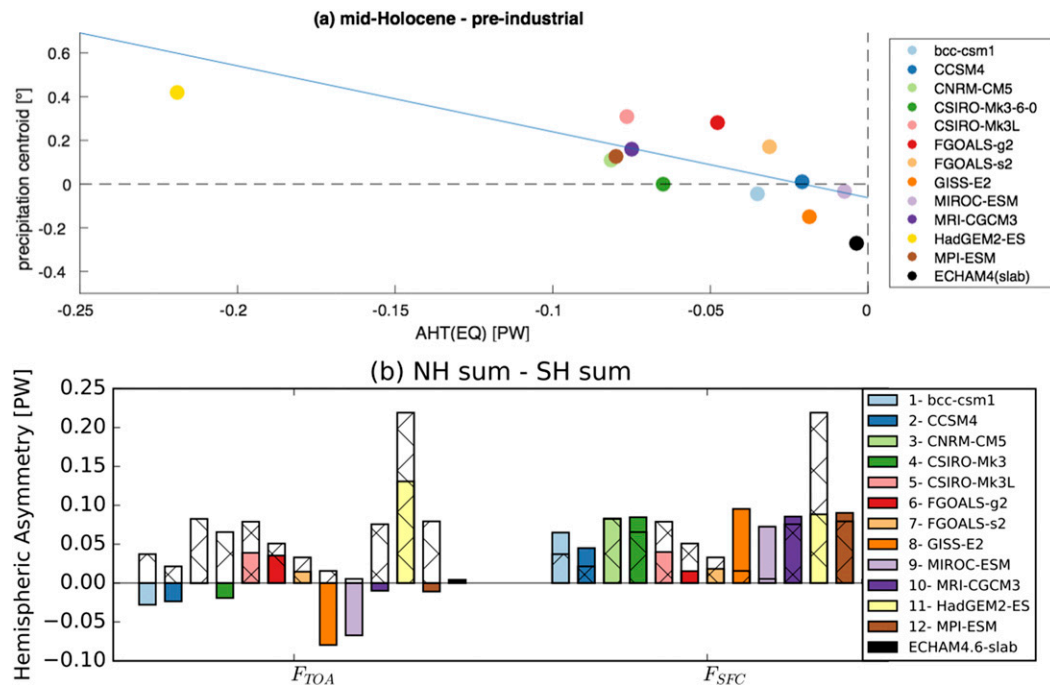


FIG. 2. (a) Scatterplot of the change (mid-Holocene minus preindustrial) in the latitude of the precipitation centroid vs the change in cross-equatorial atmospheric energy transport $\Delta AHT(EQ)$ (PW). The solid line is the least squares fit $3^\circ \text{ lat PW}^{-1}$. (b) The change in the hemispheric difference in the net hemispherically integrated energy flux into the atmosphere (colored bars) at the top of the atmosphere on the left $(1/2)[F_{TOA}]_{SH}^{NH}$ and at the surface on the right $(1/2)[F_{SFC}]_{SH}^{NH}$. For each model, the hatched bar represents the hemispheric difference in the net energy into the atmosphere; that is, the hatched bar is $-\Delta AHT(EQ)$, which is the sum of the two colored bars for each model [see Eq. (5)]. Note that at equilibrium, the change in the net surface flux in the ECHAM4.6-slab ocean model is zero. The coloring in (b) follows the key in (a).

ITCZ location change between models with a slab ocean and models with a dynamic ocean is explored in sections 3c and 4.

It is worth keeping in mind that the dominant feature of the precipitation change in the mid-Holocene is the seasonal asymmetry; the annual-mean change is just the residual of the large seasonal changes although it is consistent across the models.

b. Changes in cross-equatorial atmospheric heat transport

We use the precipitation centroid to indicate the mean ITCZ location. The precipitation centroid is defined as the latitude that delineates an equal area-averaged precipitation between 20°N and 20°S (Frierson and Hwang 2012; Donohoe et al. 2013). In 9 out of 12 PMIP3 models, the precipitation centroid shifts northward in the mid-Holocene compared with the preindustrial climate (Fig. 2a). The ensemble-mean shift is 0.11° with a spread from 0° to 0.32° (two standard deviations).

A scatterplot of the changes in precipitation centroid versus changes in $AHT(EQ)$ for the PMIP3 models shows that the change in the precipitation

centroid is anticorrelated with the change in $AHT(EQ)$, with a slope of $3.0^\circ \text{ lat PW}^{-1}$, close to that reported by Donohoe et al. (2013) for the seasonal cycle case (Fig. 2a).² Figure 2a also shows that the atmosphere transports more energy southward across the equator [$\Delta AHT(EQ) < 0$] in all PMIP3 models and is near zero in the ECHAM4.6-slab ocean model. What causes the enhanced southward $AHT(EQ)$ in the coupled simulations?

As shown in Eq. (5), in equilibrium, changes in the $AHT(EQ)$ are related to changes in the hemispheric asymmetry (defined as the spatial integral over the Northern Hemisphere minus that over the Southern Hemisphere, divided by 2) in the net energy input into the atmosphere, which, in turn, are determined by changes in the asymmetry in the hemispheric integral of F_{TOA} $\{(1/2)[F_{TOA}]_{SH}^{NH}\}$ and/or F_{SFC} $\{(1/2)[F_{SFC}]_{SH}^{NH}\}$, respectively. Decomposing the $AHT(EQ)$ into these two components shows that in almost every model

²In calculating the slope, we leave out the apparent outlier HadGEM2-ES. The slope would be $2.2^\circ \text{ lat PW}^{-1}$ if it was included.

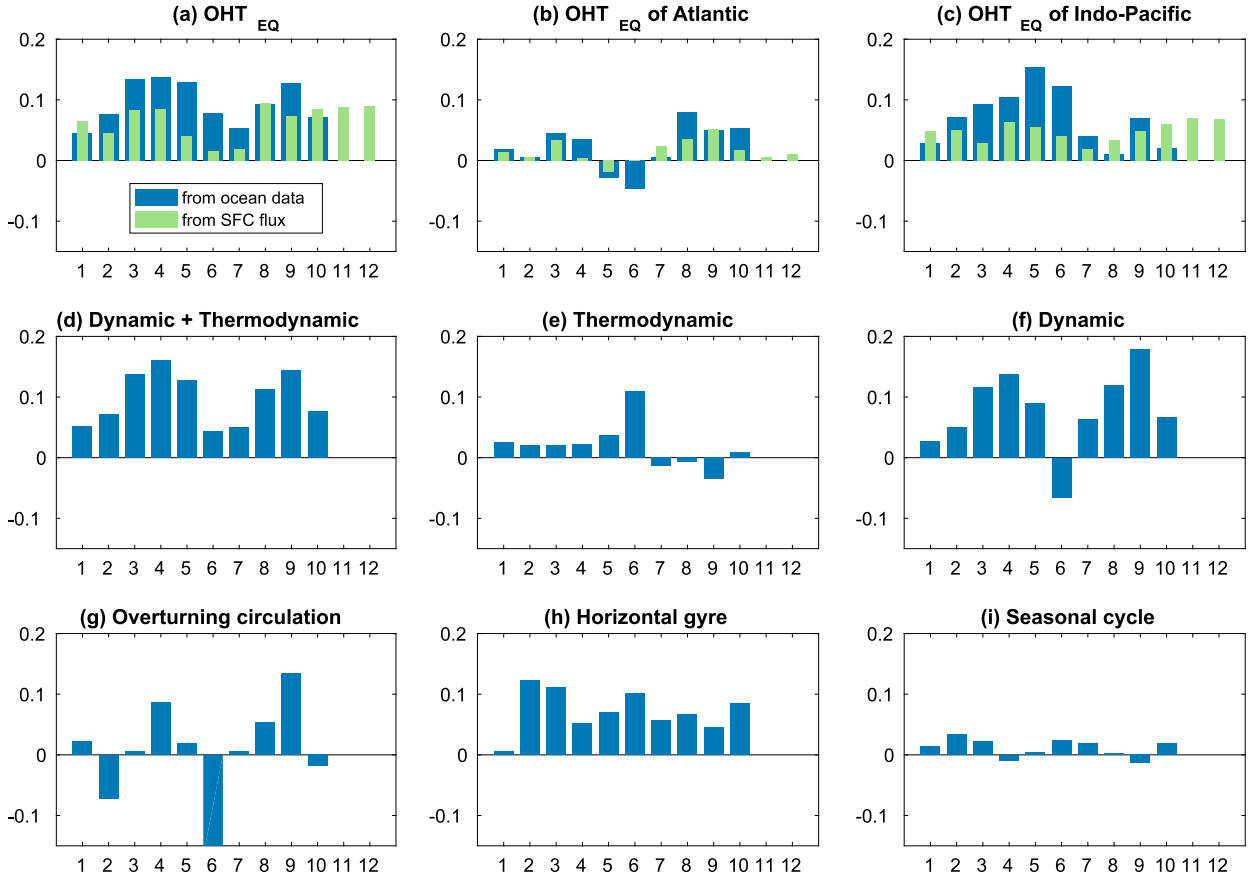


FIG. 3. Change in the cross-equatorial ocean heat transport $\Delta\text{OHT}(\text{EQ})$ (PW) between the mid-Holocene and the preindustrial for (a) the sum of the ocean basins, (b) the Atlantic basin only, and (c) the Indo-Pacific basins only. The green bars in (a)–(c) represent the results derived from the hemispheric asymmetry in the change in surface energy flux, $\Delta\text{OHT}(\text{EQ}) = -\Delta(1/2)[F_{\text{SFC}}]_{\text{SH}}^{\text{NH}}$, and blue bars denote results obtain directly from the ocean model output [Eq. (6)]. The changes in $\text{OHT}(\text{EQ})$ associated with (e) changes in the ocean temperature only and (f) changes in the ocean circulation only [see Eq. (7)]; (d) the sum of (e) and (f). The dynamic contribution shown in (f) is further broken into contributions associated with (g) the change in overturning circulation and (h) the change in gyre circulation [see Eq. (8)]. (i) The changes in the dynamic contributions due to the changes in the seasonal cycle.

(9 out of 12 models), the change in $\text{AHT}(\text{EQ})$ is predominantly due to the change in $(1/2)[F_{\text{SFC}}]_{\text{SH}}^{\text{NH}}$, the hemispheric asymmetry in energy input to the atmosphere from the surface (Fig. 2b). In all 12 PMIP3 models, the change in surface energy fluxes leads to an increase in the heating of the atmosphere in the Northern Hemisphere and a decrease in atmospheric heating in the Southern Hemisphere, resulting in a positive anomaly in $(1/2)[F_{\text{SFC}}]_{\text{SH}}^{\text{NH}}$. There is no consistent change in $(1/2)[F_{\text{TOA}}]_{\text{SH}}^{\text{NH}}$ across the models (Fig. 2b). In equilibrium, the change in $(1/2)[F_{\text{SFC}}]_{\text{SH}}^{\text{NH}}$ has to be balanced by an anomalous ocean heat transport across the equator from the Southern Hemisphere to the Northern Hemisphere. This is discussed next.

Note that there is an imbalance in global average energy budget in each model (Lucarini and Ragone 2011). This imbalance is much smaller than the change in hemispheric asymmetry between the mid-Holocene

and the preindustrial climate. It is also explicitly removed from the calculation of energy transports by subtracting the change in Northern Hemisphere top-of-the-atmosphere fluxes and surface fluxes from those in the Southern Hemisphere [Eq. (5)]. It therefore does not impact the validity of the results presented here.

c. Change in cross-equatorial oceanic heat transport

Changes in the cross-equatorial ocean heat transport $\text{OHT}(\text{EQ})$ between the mid-Holocene and preindustrial simulations are given by

$$\Delta\text{OHT}(\text{EQ}) = \rho_0 C_p \int_{-H}^0 \int_0^L [(vT)_{6K} - (vT)_{PI}] dx dz, \quad (6)$$

where ρ_0 is density of seawater, C_p is the heat capacity, and the product of $\rho_0 C_p$ is nearly constant in the ocean

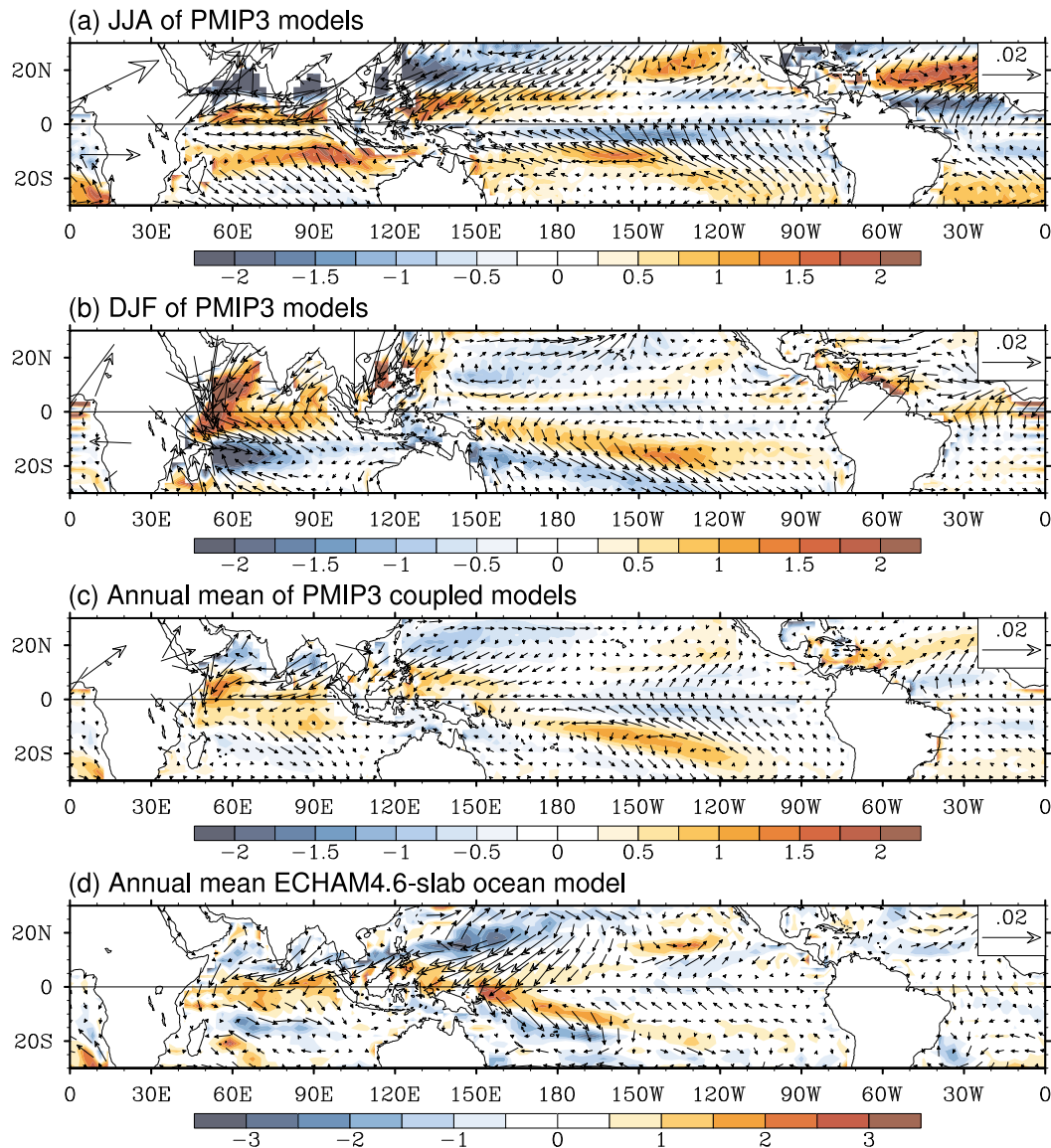


FIG. 4. Change in the annual-mean surface wind stress over the oceans (vectors; Pa) and its curl (shading; 10^{-8} N m^{-3}), mid-Holocene minus preindustrial. (a) The June–August mean change, (b) December–February mean change, and (c) annual-mean change from the multimodel mean of the PMIP3 models. (d) As in (c), but for from the ECHAM4.6-slab ocean model. Note the color bar of (d) is different from the others.

with a mean value of $4.1 \times 10^6 \text{ J m}^{-3} \text{ K}^{-1}$ used here. The variable v is meridional velocity, T is ocean potential temperature, and H and L are the depth and width of the ocean of the longitude–height cross section along the equator, respectively; subscripts 6K and PI represent the mid-Holocene simulation and the preindustrial simulation, respectively.

We use the monthly climatology of v and T to calculate $\Delta\text{OHT}(\text{EQ})$, neglecting the contribution by submonthly covarying anomalies associated with natural variability. The terms $\text{OHT}(\text{EQ})$ and $\Delta\text{OHT}(\text{EQ})$ calculated this way, however, are close to the exact answer

output by the ocean model throughout the integration (see the [appendix](#)). Note that changes in $\text{OHT}(\text{EQ})$ calculated this way are not exactly the same as those derived from the hemispheric asymmetry in the change in surface energy flux $(1/2)[F_{\text{SFC}}]_{\text{SH}}^{\text{NH}}$ (cf. blue and green bars in [Fig. 3](#)). Differences between these two estimates of $\Delta\text{OHT}(\text{EQ})$ could be due to several factors, including neglecting the contribution of submonthly covarying anomalies associated with natural variability, changes in ocean dissipation, and inaccuracies in the a posteriori calculation of ocean heat transport due to the regriding of the model output. Nonetheless, both

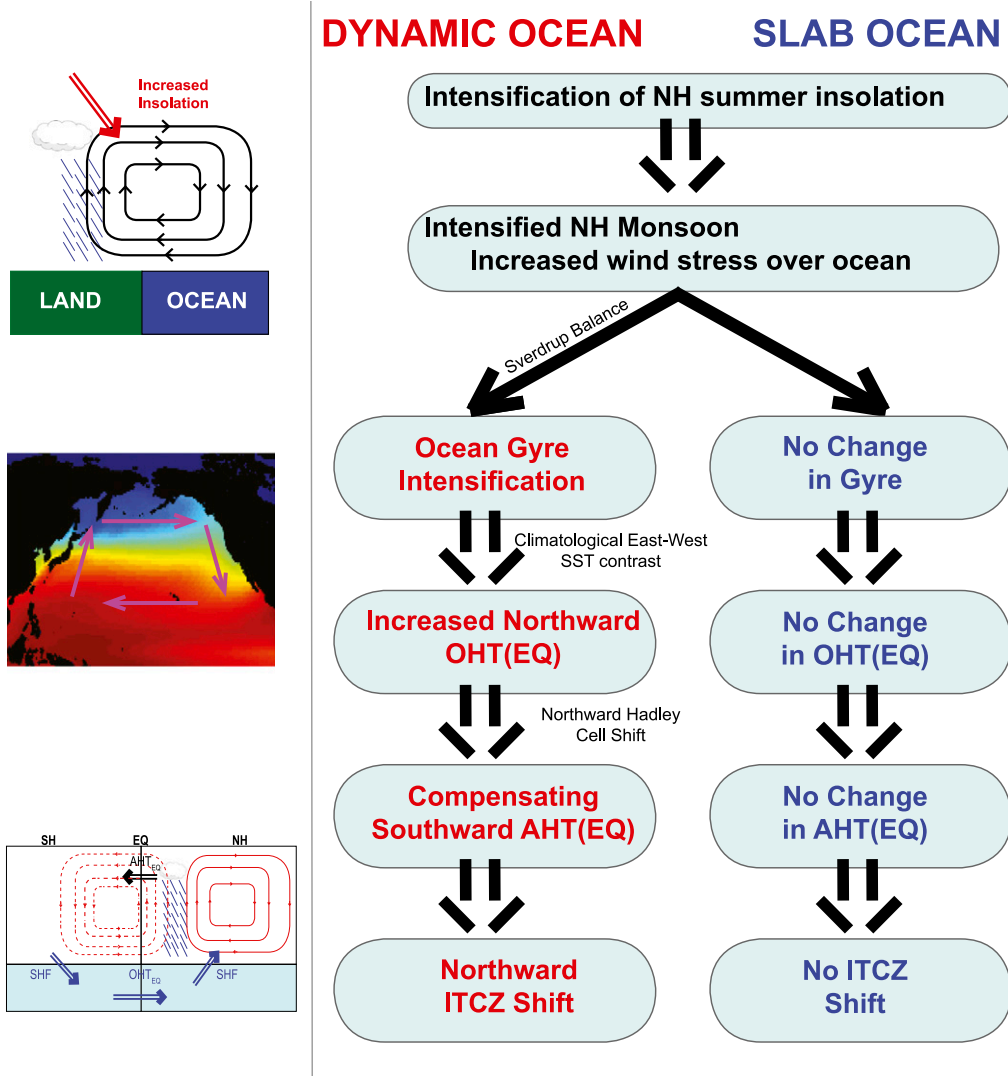


FIG. 5. Processes controlling how insolation differences between the mid-Holocene and present-day change ITCZ and AHT(EQ) differently in (center) an atmosphere–dynamic ocean model vs (right) an atmosphere–slab ocean model. Insolation differences first drive zonally and seasonally asymmetric anomalies in atmospheric circulation and hence in the surface wind stress. In the slab ocean, the changes in wind stress do not impact the ocean circulation or the heat transport. In the dynamic ocean, however, the changes in wind stress over the Indo-Pacific Ocean drive zonally asymmetric change in ocean circulation, which, acting on the zonally asymmetric climatological temperature, induces a zonally averaged anomalous northward ocean heat transport across the equator and results in anomalous heating of the Northern Hemisphere (cooling of the Southern Hemisphere). To maintain equilibrium, the atmosphere moves anomalous heat from the Northern Hemisphere to the Southern Hemisphere by shifting the Hadley cell and the attendant mean ITCZ northward.

methods yield qualitatively similar results and both methods indicate that in all 12 models the oceans are transporting more heat into the Northern Hemisphere during the mid-Holocene. The likelihood of 12 models all showing the same direction of change from simply averaging errors is 1 in 2^{11} . The robustness of increase in northward OHT(EQ) during the mid-Holocene that we have extracted using the full ensemble of

models and using multiple methods to calculate the OHT(EQ) is truly astonishing.

In the analysis that follows, we do not present results from the HadGEM2-ES because the ocean data from this model are not available from the archive. We also neglect the MPI model because the complex grid configuration makes an a posteriori calculation of OHT(EQ) unreliable.

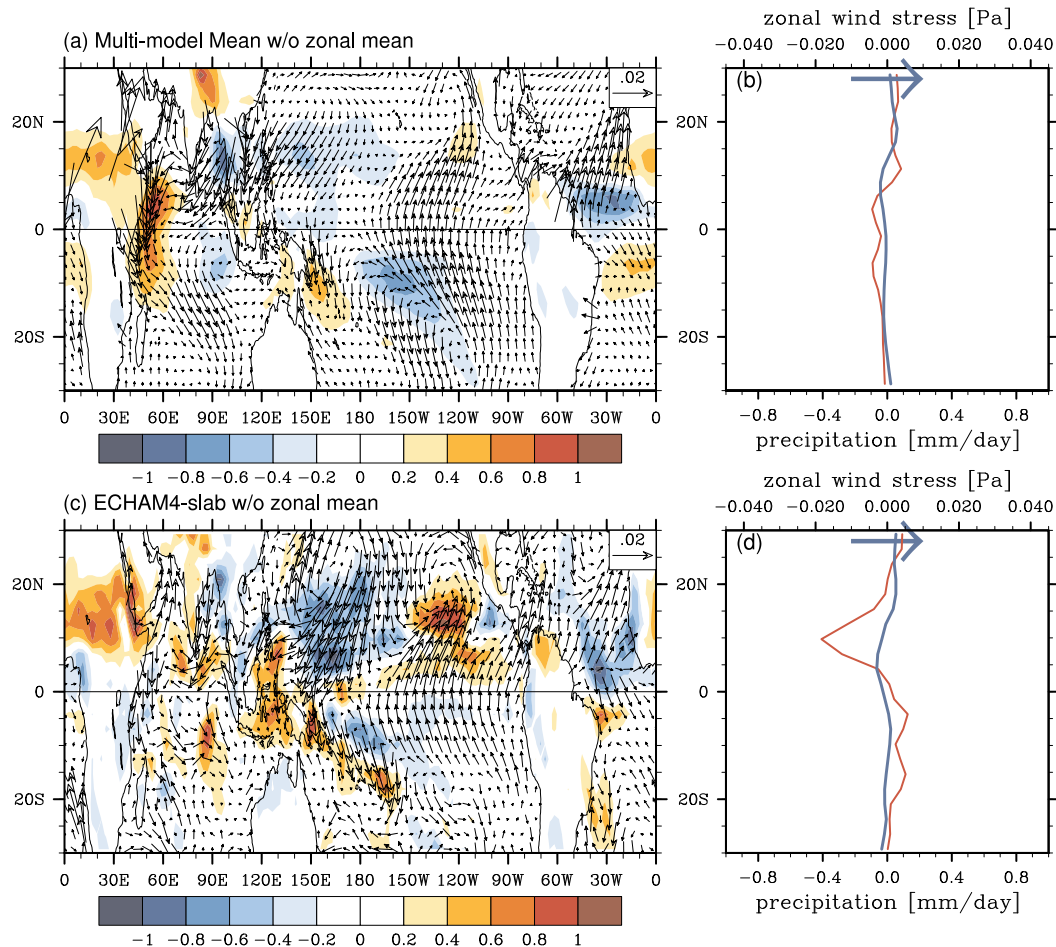


FIG. 6. (a) Change (mid-Holocene minus preindustrial) in the annual-mean surface wind stress over the oceans (vectors; Pa) and precipitation (shading; mm day⁻¹) after removal of the zonal-mean value of each latitude. Shown in (a) is the multimodel mean from the PMIP3 models. (b) The zonal-mean change in surface zonal wind stress (blue) and in precipitation (red), which, when removed from Figs. 1a and 4c, creates the figure shown in (a). (c), (d) As in (a) and (b), but for the ECHAM4.6-slab ocean model. The arrow in (b) and (d) is the reference wind stress vector used in (a) and (c).

The change in the OHT(EQ) calculated from the spatial integral of the surface heat fluxes $\{\Delta(1/2)[F_{\text{SFC}}]_{\text{SH}}^{\text{NH}}\}$ is shown in green in Fig. 3a, and those calculated from the ocean temperature and currents [Eq. (6)] are shown in blue. Both methods calculate positive OHT(EQ) change in every model (Fig. 3a). We next apply Eq. (6) and the spatial integral of surface heat fluxes to each ocean basin. In all models, the changes in the Indo-Pacific Ocean are responsible for the northward $\Delta\text{OHT}(\text{EQ})$; the contribution to $\Delta\text{OHT}(\text{EQ})$ from the Atlantic basin is highly model dependent (cf. Figs. 3b and 3c).

The change in OHT(EQ) can be further decomposed into that due to a change in the ocean circulation Δv and that due to a change in ocean temperature ΔT :

$$\begin{aligned} \Delta\text{OHT}(\text{EQ}) = & \rho_0 C_p \iint T \Delta v \, dx \, dz + \rho_0 C_p \iint v \Delta T \, dx \, dz \\ & + \rho_0 C_p \iint \Delta v \Delta T \, dx \, dz. \end{aligned} \quad (7)$$

Hereafter, we refer to the first term of the right-hand side as the dynamic contribution, and the second term as the thermodynamic contribution. Of the two, the dynamic component is the larger term in all but one model (cf. Figs. 3e and 3f). As such, there is a fair correspondence between the dynamic contribution and the total change in OHT(EQ) (cf. the blue bars in Fig. 3a with the bars in Fig. 3f). The nonlinear term [the last term of the right-hand side of Eq. (7)] is negligible, evident by comparing the sum of the dynamic and

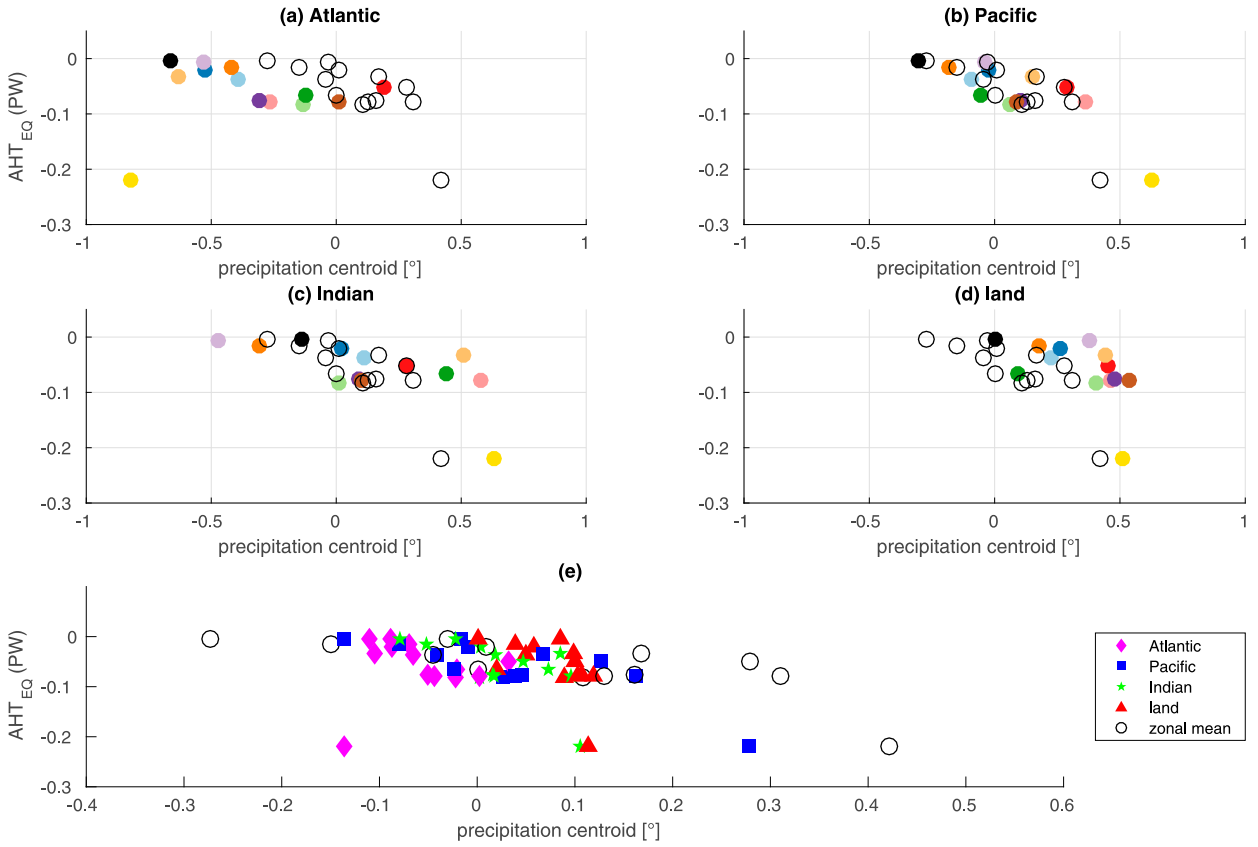


FIG. 7. Scatterplots of changes in precipitation centroid vs $\Delta AHT(EQ)$. Averages are shown over (a) the Atlantic basin, (b) the Pacific basin, (c) the Indian Ocean basin, and (d) all land. The color code in (a)–(d) is the same as the one used in Fig. 2. (e) The results in (a)–(d) are replotted with the precipitation centroid scaled by the fraction of the latitude circle occupied by the respective basin. Black unfilled circles in each panel represent the changes in the zonal-mean precipitation centroid vs $\Delta AHT(EQ)$, that is, the same as the colored dots in Fig. 2a.

thermodynamic components (Fig. 3d) with the total change in OHT(EQ) (Fig. 3a).

The dynamic term can be further broken into overturning and horizontal gyre components (Hall and Bryden 1982):

$$\rho_0 C_p \iint \overline{T' \Delta v} dx dz = \rho_0 C_p \int \overline{T' \Delta \bar{v}} dz \int dx + \rho_0 C_p \iint \overline{T' \Delta v'} dz dx, \quad (8)$$

where overbars represent the zonal mean at each vertical level and primes denote deviations from the zonal mean. The first term on the right-hand side of Eq. (8) is the contribution due to the zonal average overturning circulation, while the second term is associated with the horizontal gyres. The systematic northward change in the OHT(EQ) is clearly associated with changes in the horizontal gyre circulation (cf. Figs. 3g and 3h). Of the three ocean basins, the western Pacific is the primary contributor to the changes in OHT(EQ) associated with changes in ocean circulation. In the Indian Ocean, a weakened Somali

jet drives southward OHT(EQ) anomalies that are largely offset by northward anomalies in the interior ocean, rendering a small net dynamic contribution in Indian Ocean (not shown). Changes in the overturning circulation do not contribute to $\Delta OHT(EQ)$ in a systematic way across the models. Finally, changes in OHT(EQ) are relatively uniform through the year. The influence of the seasonal covariance of temperature and current changes is small (Fig. 3i).³

³ Figure 3i shows the importance of seasonal covariance of temperature and current changes for the change in cross-equatorial OHT estimated as follows. We first calculate the change in annual-mean heat transport using (i) the monthly climatology of currents and temperatures from the preindustrial and mid-Holocene simulations (shown in blue bars of Fig. 3a). We then estimate the change in OHT by (ii) adding the annual-mean changes (mid-Holocene minus preindustrial) in the currents and temperatures to the climatological annual cycle in the preindustrial simulation and then subtracting the preindustrial heat transport. The difference between points i and ii is plotted in Fig. 3i and shows that the changes in cross-equatorial OHT are largely independent of the changes in the seasonal cycle in currents and temperatures.

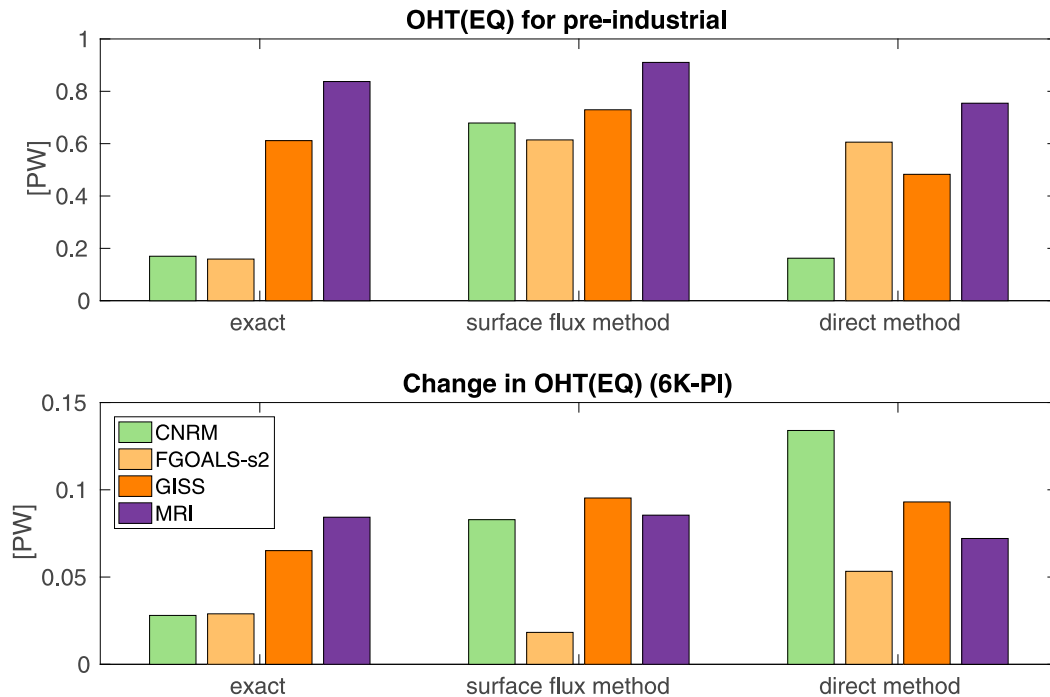


FIG. A1. (top) OHT(EQ) of the preindustrial simulation and (bottom) the difference in OHT(EQ) between preindustrial and mid-Holocene Δ OHT(EQ), calculated using three methods. In the figure, exact denotes OHT(EQ) calculated by the model and output during the simulation (the exact answer); the surface flux method refers to OHT(EQ) derived from the hemispheric asymmetry in the change in surface energy flux, Δ OHT(EQ) = $-\Delta(1/2)[F_{\text{SFC}}]_{\text{SH}}^{\text{NH}}$; and direct method refers to the calculation of OHT(EQ) from ocean current and temperature output from the model.

The changes in ocean circulation and hence OHT(EQ) are primarily due to changes in wind stress in the Indo-Pacific region that have a common pattern across nearly all of the models. Figure 4c shows the multimodel-mean change in the annual-mean wind stress in the PMIP3 models associated with the mid-Holocene compared to the present. The pattern seen in Fig. 4c is common to all the PMIP3 models we examined (cf. Figs. 4c, 4d and Fig. A2). Over the Indian Ocean and far western Pacific, enhanced trades (easterly stress anomalies) are seen along and to the north of the equator in 10 of 12 models (including the ECHAM4.6 model coupled to a slab), resulting in a positive wind stress curl near the equator. According to Sverdrup transport theory, the positive curl in the western Indo-Pacific basin drives northward movement of water in the upper ocean. Although there are negative curl anomalies in the eastern Pacific, which drive southward movement of water in the upper ocean because the upper-ocean water in the western Indo-Pacific basin is warmer than that in the eastern Pacific, the anomalous gyre circulation produces a northward zonally averaged ocean heat transport anomaly across the equator. The role of surface wind stress and hence horizontal gyre in generating the anomalous ocean

heat transport is also found by Braconnot et al. (2000) using the coupled version of L'Institut Pierre-Simon Laplace (IPSL) model.

From the analysis above, it is clear that the increase in northward OHT(EQ) in the mid-Holocene—seen in all of the 10 models coupled to a dynamic ocean—is due to changes in wind stress in the western Pacific. These wind anomalies are seen in nearly every PMIP3 model (which employ dynamical ocean models), as well as in an ECHAM4.6–slab ocean model (Fig. 4d), and hence are independent of the ocean circulation changes. Indeed, the wind changes are a monsoonal response to the orbitally driven changes in insolation during the mid-Holocene (Battisti et al. 2014; Liu and Battisti 2015). In the Northern Hemisphere, the stronger summer insolation shifts convection from the ocean to the land in the Indian Ocean basin, resulting in annually averaged easterly anomalies in the tropical Indian Ocean basin and the western Pacific Ocean. In the Southern Hemisphere, the weaker summer insolation shifts convection from the land to the ocean, resulting in annually averaged westerly anomalies in the tropical Indian Ocean basin and the western Pacific Ocean (Figs. 4a,b).

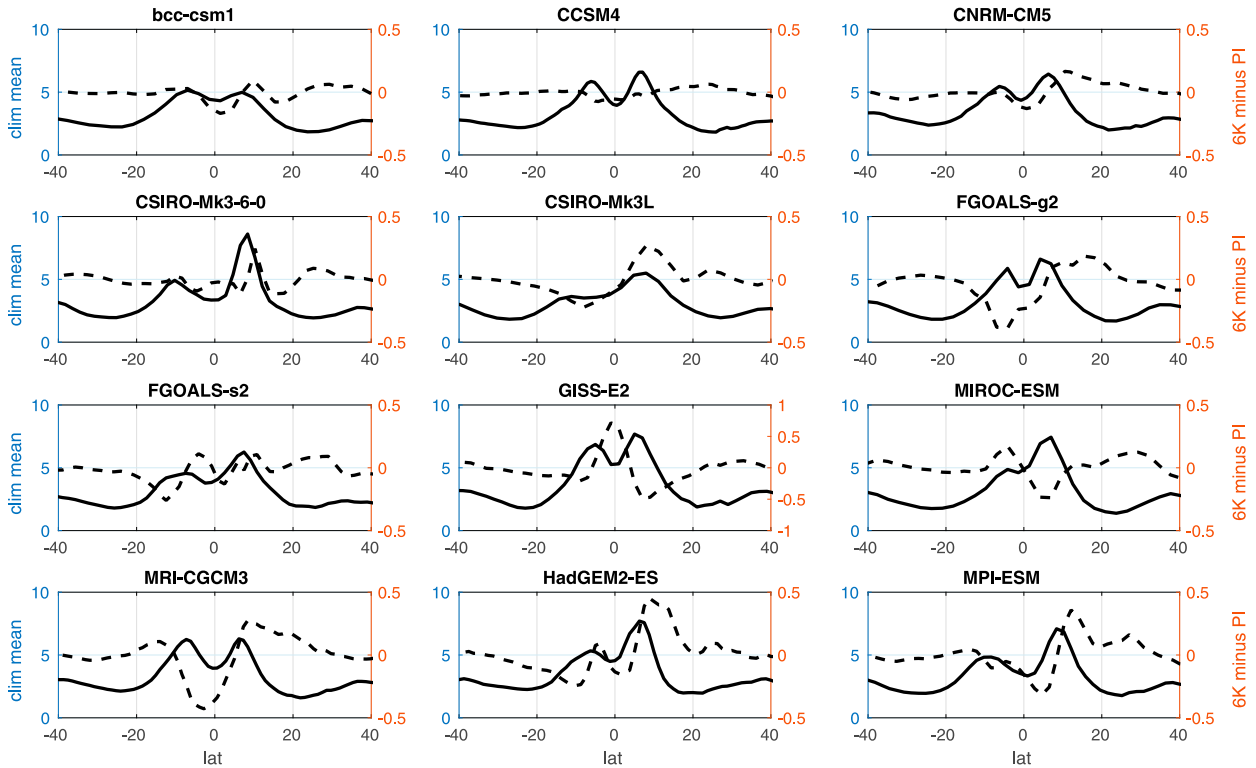


FIG. A2. The climatological annual-mean precipitation in the preindustrial experiment (solid line; mm day^{-1}) and the change in annual-mean precipitation (mid-Holocene minus preindustrial; dashed line; mm day^{-1}) for each PMIP3 model.

4. A mechanistic model of the change in mean ITCZ and in the cross-equatorial ocean heat transport

In the ECHAM4.6 model that employs a slab ocean, insolation changes are responsible for a southward shift of the mean ITCZ. In most of the models (9 out of 12) with a dynamic ocean, however, there is a northward shift in ITCZ. The analyses presented in the previous section suggest changes in ocean circulation play a crucial role in the changes in the interhemispheric energy transport associated with insolation forcing. The mechanism responsible for the different responses in the model that employs the slab ocean and all of the models that employ dynamical oceans is shown schematically in Fig. 5 and is summarized as follows.

In the previous section, we showed that insolation differences between the mid-Holocene and today drive similar changes in precipitation and very similar changes in tropical atmospheric circulation in both the models with and without a dynamic ocean (Hsu et al. 2010; K. Chamales et al. 2017, manuscript submitted to *Geophys. Res. Lett.*). The changes in precipitation and atmospheric circulation are overwhelmingly zonally asymmetric in all of the models (cf. Fig. 1 with Fig. 6); indeed, the zonally averaged wind stress anomalies are less than 20% of the typical wind stress

anomaly. The robust changes in atmospheric circulation over the Indian and Pacific Oceans feature a change in the wind stress curl in the equatorial regions of these ocean basins that, acting on a zonally asymmetric climatological temperature structure, results in basin-averaged northward increase in ocean heat transport across the equator, particularly in the tropical Pacific. The atmosphere, in turn, experiences an increase in heat absorbed in the Northern Hemisphere that is not completely compensated for by changes in the top-of-the-atmosphere radiation. Hence, to maintain equilibrium, the atmosphere must move anomalous heat into the Southern Hemisphere. Since the atmosphere moves energy across the equator overwhelmingly by the zonally averaged overturning circulation, this requires the zonally averaged Hadley circulation and attendant ITCZ to shift northward. In contrast, in the ECHAM4.6 model coupled to a slab ocean, there is a southward shift in the ITCZ and an anomalous increase in AHT(EQ). Radiative feedbacks (i.e., radiation changes in response to changes in clouds and water vapor) in response to mid-Holocene insolation changes result in a radiative input to the Southern Hemisphere $\{\Delta(1/2)[F_{\text{TOA}}]_{\text{SH}}^{\text{NH}} < 0\}$ that shift the mean ITCZ southward.

The mechanism discussed above—whereby enhanced wind-driven northward ocean heat transport induces a

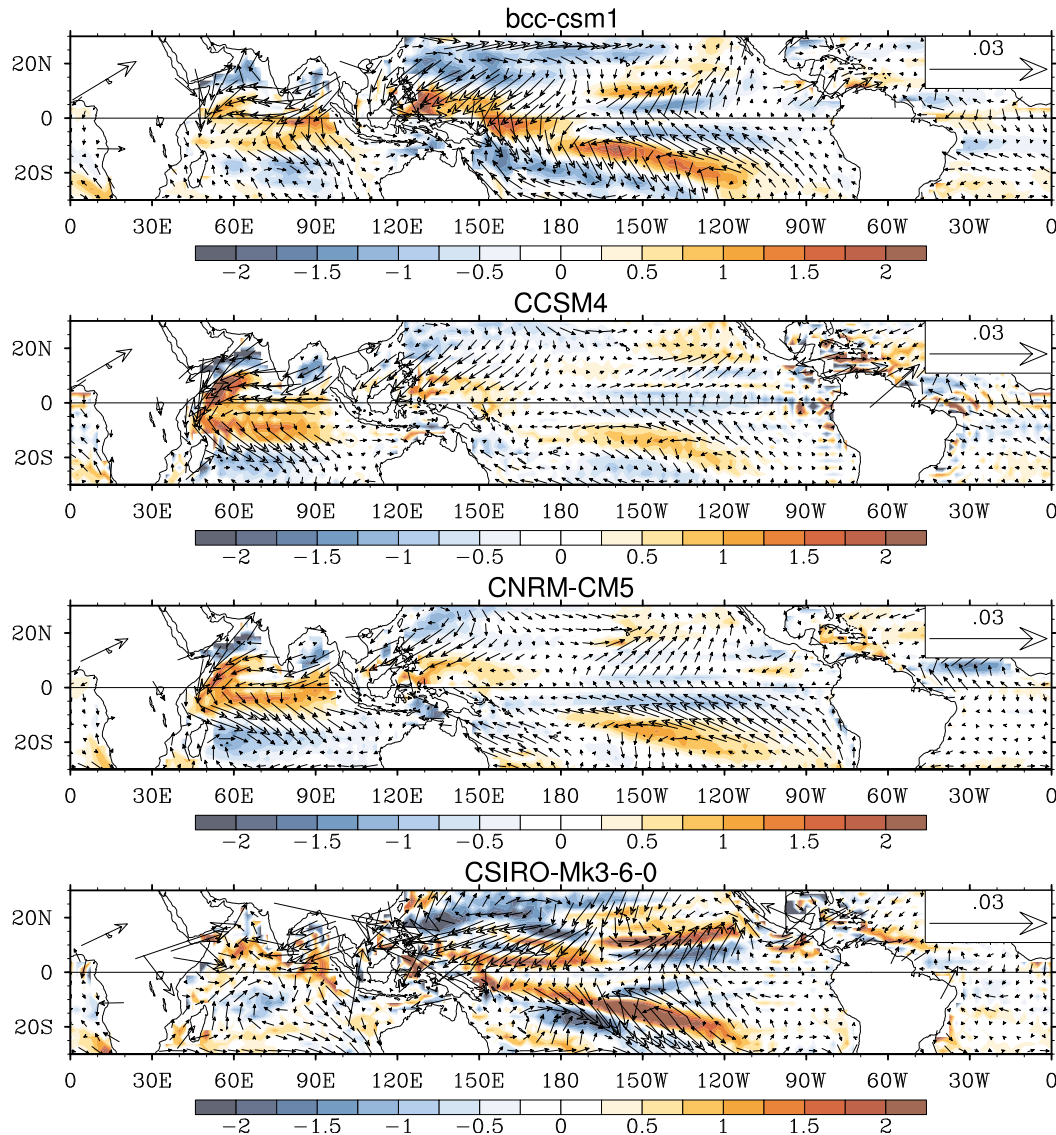


FIG. A3. Changes (mid-Holocene minus preindustrial) in the annual-mean surface wind stress (vectors; Pa) and wind stress curl (shading; 10^{-8} N m^{-3}) for each PMIP3 model.

northward shift in the Hadley cell and ITCZ—explains the robust ensemble-mean, northward ITCZ shift from the perspective of the energetic framework of ITCZ shifts. While the northward ocean energy transport increases in all models considered here, there are two main reasons that individual model simulations show varying magnitudes and directions of ITCZ shifts (Fig. 2): (i) the hemispheric contrast of top-of-the-atmosphere radiative changes varies in sign and direction between models—a nearly equal number of models simulating anomalous radiative input in to the Northern Hemisphere as those that simulate anomalous energy input to the Southern Hemisphere (left side of Fig. 2b)—and (ii) the relationship between AHT(EQ) and precipitation centroid explains a significant portion of the

ensemble average and spread in ITCZ shifts but is far from perfect (i.e., the individual dots do not fall exactly on the a straight line through the origin in Fig. 2a). The latter could result from changes in static stability or local precipitation changes projecting onto the zonal mean precipitation without concomitant changes in the Hadley cell. As a result, even though the enhanced northward ocean transport is seen in every model, it is not a useful predictor of ITCZ shifts in a given climate model.

5. Conclusions and discussion

Orbitally induced insolation changes impact tropical precipitation dramatically. We have demonstrated that, in

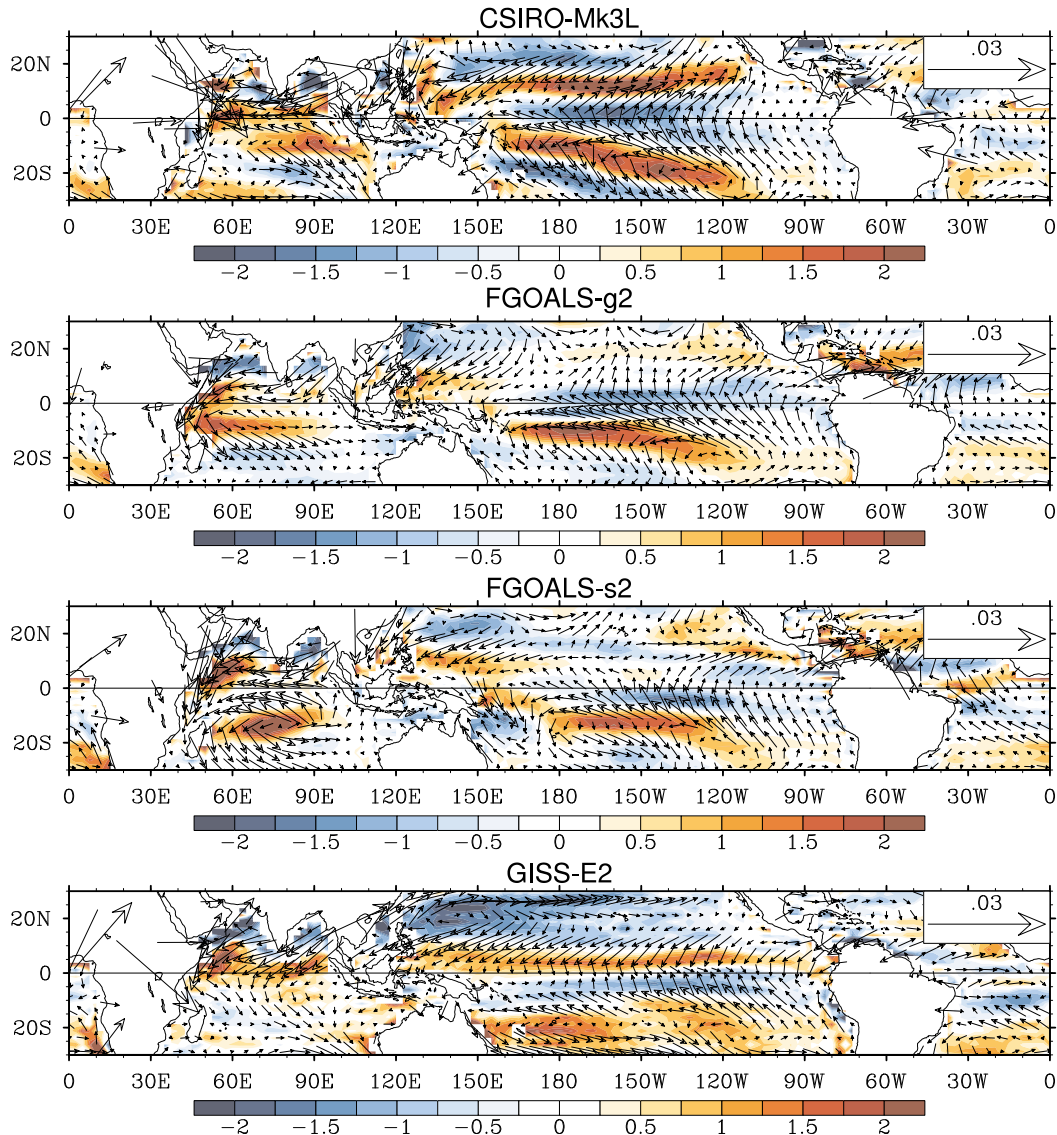


FIG. A3. (Continued)

addition to the intensification of the Northern Hemisphere monsoon and (not emphasized) the weakening of the Southern Hemisphere monsoon in the mid-Holocene, in all 12 PMIP3 climate models that employ a dynamic ocean, the northward OHT(EQ) is enhanced, and the southward AHT(EQ) is also enhanced as a result. In contrast, in models without interactive oceans, AHT(EQ) is nearly unchanged. The change in cross-equatorial atmospheric heat transport is accomplished by the Hadley cell; hence, the mean ITCZ shifts northward in the models with an interactive ocean.

The increase in northward OHT(EQ) is accomplished by changes in the upper-ocean gyre circulations in the Indo-Pacific and particularly the Pacific Ocean; there is no systematic change in the ocean heat transport in the

Atlantic Ocean. The changes in the wind stress that drive the anomalous gyre circulations are independent of whether the models have a dynamical ocean. The surface circulation pattern that drives the gyre circulation changes is clearly seen in all but one of the 12 models examined; it is also simulated by the ECHAM4.6 coupled to a slab ocean model used in this study. However, the impact of this wind stress change on the mean ITCZ varies between coupled simulations and slab ocean simulations; in coupled simulations the wind stress changes spin up the tropical Pacific Gyre, enhancing the northward ocean heat transport and demanding a northward Hadley cell and ITCZ response, whereas this same mechanism is absent in slab ocean simulations. The ITCZ shift in a minority of

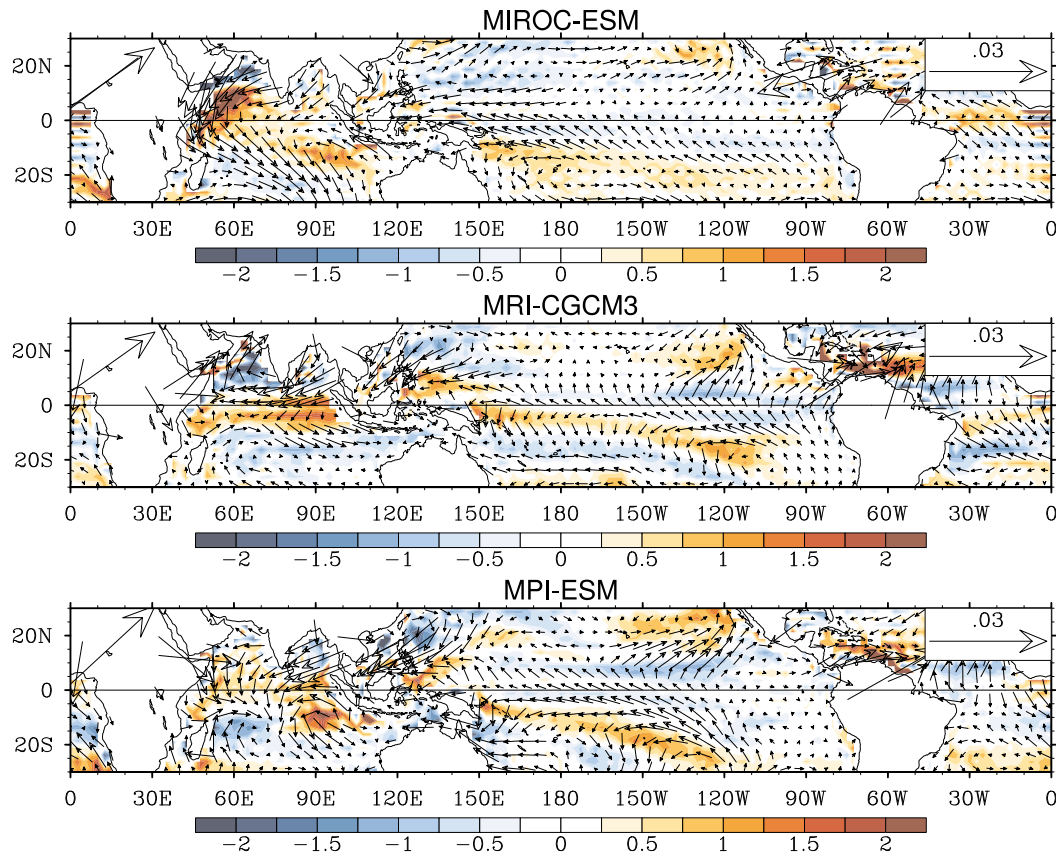


FIG. A3. (Continued)

models (BCC_CSM1.1, MIROC-ESM, and GISS-E2) is southward—contrary to the northward shift expected from the above mechanism—due to both radiative feedbacks and departures from the energetic framework. However, the robust northward ITCZ shift seen in the ensemble of PMIP3 mid-Holocene simulations would not exist without the coupling between the wind stress changes and the ocean circulation. We speculate that an ensemble of slab ocean mid-Holocene simulations would exhibit intermodel differences in the ITCZ shift with no significant ensemble-mean shift.

Many modeling studies examining the impact of forcing on the ITCZ employ atmospheric models coupled to slab ocean models. However, results from our study demonstrate that—at least for changes in insolation—the response of ITCZ is mainly due to dynamical changes in the ocean that are driven by the overwhelmingly zonally asymmetric atmospheric circulation anomalies that are, in turn, independent of the ocean circulation changes [the latter result is also found in several other studies (Clement et al. 2004; Hsu et al. 2010; McGee et al. 2014; Battisti et al. 2014; Liu and Battisti 2015)].

We note that the difference in insolation between the mid-Holocene and preindustrial periods induce changes in atmospheric circulation in the tropical Indian and Pacific Oceans that are common to almost all models [cf. Figs. 4 and A3], regardless of whether dynamical changes in the ocean are considered. The pattern of insolation-induced precipitation changes over tropical land regions is also common to most of the models but less so than the circulation changes, particularly over the ocean basins (cf. Figs. 1a and 1b). This result has been reported in a previous study of the response of the circulation and precipitation of the Maritime Continent to increasing CO₂ (Vimont et al. 2010) and is expected. Monsoon circulations and precipitation are intimately related to the near-surface moist static energy (Prive and Plumb 2007a,b; Bordoni and Schneider 2008; Boos and Kuang 2010). The dynamical scale associated with changes in the monsoon circulations due to changes in near-surface moist static energy is the equatorial Rossby radius, which is $\sim 10^6$ m; in contrast, the storms that release the energy that drives the monsoon circulations are at least an order of magnitude smaller than the spatial scale associated with the monsoon circulations. Hence,

the relevant heating for the monsoon circulations is the aggregate of the precipitating elements: the details of the distribution of precipitation are secondary for setting the circulation response. In addition, the dynamics associated with the monsoon circulations is explicitly resolved in climate models, while the convective elements that convert the surface energy to atmospheric heating are parameterized.

Finally, although the focus of our paper is on understanding the zonal-mean response to insolation forcing, it is important to keep in mind that the dominant changes in tropical climate [precipitation, temperature (not shown), and wind] are zonally asymmetric. This can be seen, for example, in the asymmetry of the precipitation changes (Fig. 1) as well as by comparing the maps of precipitation and wind stress change with and without the zonal mean removed (cf. Figs. 1, 4, and 6); the figures are nearly identical. Indeed, although the global zonal average precipitation in the deep tropics (represented by the precipitation centroid) moves northward in response to mid-Holocene insolation compared to preindustrial insolation, changes in ITCZ are accomplished by the sum of differential changes in the zonal average precipitation over each ocean basin and over the land regions (Fig. 7); on average the zonal average precipitation over the Atlantic Ocean moves southward, while that over land moves northward (over the Indian and Pacific Oceans, the sign of the meridional displacement is not a robust model result). We note that a follow-up study (A. Atwood et al. 2017, unpublished manuscript) shows that the zonally averaged ITCZ displacement due to other forcings (volcanic, freshwater, CO₂, and land ice) is also accomplished by a sum of differential displacements in the zonal-mean precipitation averaged over each basin. The implications for inferring larger-scale climate changes from local proxy records of precipitation are apparent.

Acknowledgments. We acknowledge the World Climate Research Programme's Working Group on Coupled Modelling, which is responsible for CMIP, and we thank the climate modeling groups (listed in Table 1 of this paper) for producing and making available their model output. For CMIP the U.S. Department of Energy's Program for Climate Model Diagnosis and Intercomparison provides coordinating support and led development of software infrastructure in partnership with the Global Organization for Earth System Science Portals. We thank Dr. Pascale Braconnot and two other anonymous reviewers whose comments greatly helped improve the manuscript. XL thanks Drs. Dargan Frierson and Chris Bretherton for helpful conversations. DSB and XL were supported by grants from the National Science Foundation

(Division of Earth Sciences Continental Dynamics Programs Award 1210920 and Frontiers in Earth System Dynamics Award 1338694); AD was supported on a SEED grant from the Applied Physics Lab at the University of Washington.

APPENDIX

The Estimate of OHT(EQ)

We calculate the changes in cross-equatorial ocean heat transport OHT(EQ) using three methods to assess the reliability of calculating OHT(EQ) from the monthly mean climatological fields. Figure A1 shows Δ OHT(EQ): 1) directly output by the ocean throughout the integration and so calculated on the model grid and at the model time step (the so-called exact calculation), 2) calculated as the hemispheric differences in surface energy flux, and 3) calculated using the monthly averaged currents and temperature that were output from the model, that is, Eq. (6). Calculations were done for the four models that reported the exact answer (CNRM-CM5, FGOALS-s2, GISS-E2-R, and MRI-CGCM3). For three of the four models, calculating OHT(EQ) from the monthly mean climatological fields gives a very similar answer to the exact answer output from the ocean models (differences are less than 0.1 PW; Fig. A1). Furthermore, for all four models, OHT(EQ) increases in the mid-Holocene compared to the modern climate, regardless of the method used to calculate OHT(EQ) (there are no negative values in Fig. A1, bottom).

Our results are also robust in the sense that (i) the northward shift of the mean ITCZ in the mid-Holocene relative to the preindustrial simulation is seen in the majority (9 out of 12) of the models (Fig. A2); and (ii) the changes in the annual-mean surface wind stress and its curl in the tropical Indian and Pacific Oceans seen in the ensemble mean result (Fig. 4) are common to almost all the models (Fig. A3).

REFERENCES

- Arbuszewski, J. A., P. B. deMenocal, C. Cléroux, L. Bradtmiller, and Alan Mix, 2013: Meridional shifts of the Atlantic intertropical convergence zone since the Last Glacial Maximum. *Nat. Geosci.*, **6**, 959–962, doi:10.1038/ngeo1961.
- Bao, Q., and Coauthors, 2013: The Flexible Global Ocean-Atmosphere-Land System Model, spectral version 2: FGOALS-s2. *Adv. Atmos. Sci.*, **30**, 561–576, doi:10.1007/s00376-012-2113-9.
- Bartlein, P., and Coauthors, 2011: Pollen-based continental climate reconstructions at 6 and 21 ka: A global synthesis. *Climate Dyn.*, **37**, 775–802, doi:10.1007/s00382-010-0904-1.
- Battisti, D., Q. Ding, and G. Roe, 2014: Coherent pan-Asian climatic and isotopic response to orbital forcing of tropical

- insolation. *J. Geophys. Res. Atmos.*, **119**, 11 997–12 020, doi:10.1002/2014JD021960.
- Boos, W. R., and Z. Kuang, 2010: Dominant control of the South Asian monsoon by orographic insulation versus plateau heating. *Nature*, **463**, 218–222, doi:10.1038/nature08707.
- , and R. L. Korty, 2016: Regional energy budget control of the intertropical convergence zone and application to mid-Holocene rainfall. *Nat. Geosci.*, **9**, 892–897, doi:10.1038/ngeo2833.
- Bordoni, S., and T. Schneider, 2008: Monsoons as eddy-mediated regime transitions of the tropical overturning circulation. *Nat. Geosci.*, **1**, 515–519, doi:10.1038/ngeo248.
- Bosmans, J., S. Drijfhout, E. Tuenter, L. Lourens, F. Hilgen, and S. Weber, 2012: Monsoonal response to mid-Holocene orbital forcing in a high resolution GCM. *Climate Past*, **8**, 723–740, doi:10.5194/cp-8-723-2012.
- Braconnot, P., O. Marti, S. Joussaume, and Y. Leclainche, 2000: Ocean feedback in response to 6 kyr BP insolation. *J. Climate*, **13**, 1537–1553, doi:10.1175/1520-0442(2000)013<1537:OFIRTK>2.0.CO;2.
- , and Coauthors, 2007a: Results of PMIP2 coupled simulations of the mid-Holocene and Last Glacial Maximum—Part 1: Experiments and large-scale features. *Climate Past*, **3**, 261–277, doi:10.5194/cp-3-261-2007.
- , and Coauthors, 2007b: Results of PMIP2 coupled simulations of the mid-Holocene and Last Glacial Maximum—Part 2: Feedbacks with emphasis on the location of the ITCZ and mid- and high latitudes heat budget. *Climate Past*, **3**, 279–296, doi:10.5194/cp-3-279-2007.
- , S. P. Harrison, M. Kageyama, P. J. Bartlein, V. Masson-Delmotte, A. Abe-Ouchi, B. Otto-Bliesner, and Y. Zhao, 2012: Evaluation of climate models using palaeoclimatic data. *Nat. Climate Change*, **2**, 417–424, doi:10.1038/nclimate1456.
- Clement, A., A. Hall, and A. Broccoli, 2004: The importance of precessional signals in the tropical climate. *Climate Dyn.*, **22**, 327–341, doi:10.1007/s00382-003-0375-8.
- Collins, J. A., and Coauthors, 2011a: Interhemispheric symmetry of the tropical African rainbelt over the past 23,000 years. *Nat. Geosci.*, **4**, 42–45, doi:10.1038/ngeo1039.
- Collins, W., and Coauthors, 2011b: Development and evaluation of an Earth-system model—HadGEM2. *Geosci. Model Dev.*, **4**, 1051–1075, doi:10.5194/gmd-4-1051-2011.
- Donohoe, A., J. Marshall, D. Ferreira, and D. Mcgee, 2013: The relationship between ITCZ location and cross-equatorial atmospheric heat transport: From the seasonal cycle to the Last Glacial Maximum. *J. Climate*, **26**, 3597–3618, doi:10.1175/JCLI-D-12-00467.1.
- Frierson, D. M., and Y.-T. Hwang, 2012: Extratropical influence on ITCZ shifts in slab ocean simulations of global warming. *J. Climate*, **25**, 720–733, doi:10.1175/JCLI-D-11-00116.1.
- , and Coauthors, 2013: Contribution of ocean overturning circulation to tropical rainfall peak in the Northern Hemisphere. *Nat. Geosci.*, **6**, 940–944, doi:10.1038/ngeo1987.
- Gent, P. R., and Coauthors, 2011: The Community Climate System Model version 4. *J. Climate*, **24**, 4973–4991, doi:10.1175/2011JCLI4083.1.
- Hall, M. M., and H. L. Bryden, 1982: Direct estimates and mechanisms of ocean heat transport. *Deep-Sea Res.*, **29A**, 339–359, doi:10.1016/0198-0149(82)90099-1.
- Haug, G. H., K. A. Hughen, D. M. Sigman, L. C. Peterson, and U. Röhl, 2001: Southward migration of the intertropical convergence zone through the Holocene. *Science*, **293**, 1304–1308, doi:10.1126/science.1059725.
- Hsu, Y.-H., C. Chou, and K.-Y. Wei, 2010: Land–ocean asymmetry of tropical precipitation changes in the mid-Holocene. *J. Climate*, **23**, 4133–4151, doi:10.1175/2010JCLI3392.1.
- Jolly, D., S. Harrison, B. Damnati, and R. Bonnefille, 1998: Simulated climate and biomes of Africa during the late Quaternary: Comparison with pollen and lake status data. *Quat. Sci. Rev.*, **17**, 629–657, doi:10.1016/S0277-3791(98)00015-8.
- Jones, C., and Coauthors, 2011: The HadGEM2-ES implementation of CMIP5 centennial simulations. *Geosci. Model Dev.*, **4**, 543–570, doi:10.5194/gmd-4-543-2011.
- Joussaume, S., and Coauthors, 1999: Monsoon changes for 6000 years ago: Results of 18 simulations from the Paleoclimate Modeling Intercomparison Project (PMIP). *Geophys. Res. Lett.*, **26**, 859–862, doi:10.1029/1999GL900126.
- Kutzbach, J. E., and P. J. Guetter, 1986: The influence of changing orbital parameters and surface boundary conditions on climate simulations for the past 18 000 years. *J. Atmos. Sci.*, **43**, 1726–1759, doi:10.1175/1520-0469(1986)043<1726:TIOCOP>2.0.CO;2.
- LeGrande, A. N., and G. A. Schmidt, 2009: Sources of Holocene variability of oxygen isotopes in paleoclimate archives. *Climate Past*, **5**, 441–455, doi:10.5194/cp-5-441-2009.
- Li, L., and Coauthors, 2013: The flexible global ocean-atmosphere-land system model, grid-point version 2: FGOALS-g2. *Adv. Atmos. Sci.*, **30**, 543–560, doi:10.1007/s00376-012-2140-6.
- Liu, X., and D. S. Battisti, 2015: The influence of orbital forcing of tropical insolation on the climate and isotopic composition of precipitation in South America. *J. Climate*, **28**, 4841–4862, doi:10.1175/JCLI-D-14-00639.1.
- Lucarini, V., and F. Ragone, 2011: Energetics of climate models: Net energy balance and meridional enthalpy transport. *Rev. Geophys.*, **49**, RG1001, doi:10.1029/2009RG000323.
- Mantsis, D. F., A. C. Clement, A. J. Broccoli, and M. P. Erb, 2011: Climate feedbacks in response to changes in obliquity. *J. Climate*, **24**, 2830–2845, doi:10.1175/2010JCLI3986.1.
- Marsland, S. J., H. Haak, J. H. Jungclaus, M. Latif, and F. Röske, 2003: The Max-Planck-Institute global ocean/sea ice model with orthogonal curvilinear coordinates. *Ocean Modell.*, **5**, 91–127, doi:10.1016/S1463-5003(02)00015-X.
- Martin, G. M., and Coauthors, 2011: The HadGEM2 family of Met Office Unified Model climate configurations. *Geosci. Model Dev.*, **4**, 723–757, doi:10.5194/gmd-4-723-2011.
- McGee, D., A. Donohoe, J. Marshall, and D. Ferreira, 2014: Changes in ITCZ location and cross-equatorial heat transport at the Last Glacial Maximum, Heinrich Stadial 1, and the mid-Holocene. *Earth Planet. Sci. Lett.*, **390**, 69–79, doi:10.1016/j.epsl.2013.12.043.
- Paillard, D., 2010: Climate and the orbital parameters of the earth. *C. R. Geosci.*, **342**, 273–285, doi:10.1016/j.crte.2009.12.006.
- Phipps, S., L. Rotstayn, H. Gordon, J. Roberts, A. Hirst, and W. Budd, 2011: The CSIRO Mk3L climate system model version 1.0—Part 1: Description and evaluation. *Geosci. Model Dev.*, **4**, 483–509, doi:10.5194/gmd-4-483-2011.
- Prado, L. F., I. Wainer, and C. M. Chiessi, 2013: Mid-Holocene PMIP3/CMIP5 model results: Intercomparison for the South American monsoon system. *Holocene*, **23**, 1915–1920, doi:10.1177/0959683613505336.
- Prive, N. C., and R. A. Plumb, 2007a: Monsoon dynamics with interactive forcing. Part I: Axisymmetric studies. *J. Atmos. Sci.*, **64**, 1417–1430, doi:10.1175/JAS3916.1.
- , and —, 2007b: Monsoon dynamics with interactive forcing. Part II: Impact of eddies and asymmetric geometries. *J. Atmos. Sci.*, **64**, 1431–1442, doi:10.1175/JAS3917.1.

- Raddatz, T., and Coauthors, 2007: Will the tropical land biosphere dominate the climate–carbon cycle feedback during the twenty-first century? *Climate Dyn.*, **29**, 565–574, doi:10.1007/s00382-007-0247-8.
- Rotstayn, L. D., M. A. Collier, M. R. Dix, Y. Feng, H. B. Gordon, S. P. O’Farrell, I. N. Smith, and J. Syktus, 2010: Improved simulation of Australian climate and ENSO-related rainfall variability in a global climate model with an interactive aerosol treatment. *Int. J. Climatol.*, **30**, 1067–1088, doi:10.1002/joc.1952.
- Schmidt, G. A., and Coauthors, 2006: Present-day atmospheric simulations using GISS ModelE: Comparison to in situ, satellite, and reanalysis data. *J. Climate*, **19**, 153–192, doi:10.1175/JCLI3612.1.
- Schneider, T., T. Bischoff, and G. H. Haug, 2014: Migrations and dynamics of the intertropical convergence zone. *Nature*, **513**, 45–53, doi:10.1038/nature13636.
- Street, F. A., and A. Grove, 1976: Environmental and climatic implications of late Quaternary lake-level fluctuations in Africa. *Nature*, **261**, 385–390, doi:10.1038/261385a0.
- Taylor, K. E., R. J. Stouffer, and G. A. Meehl, 2012: An overview of CMIP5 and the experiment design. *Bull. Amer. Meteor. Soc.*, **93**, 485–498, doi:10.1175/BAMS-D-11-00094.1.
- Vimont, D. J., D. S. Battisti, and R. L. Naylor, 2010: Downscaling Indonesian precipitation using large-scale meteorological fields. *Int. J. Climatol.*, **30**, 1706–1722, doi:10.1002/joc.2010.
- Voltaire, A., and Coauthors, 2013: The CNRM-CM5.1 global climate model: Description and basic evaluation. *Climate Dyn.*, **40**, 2091–2121, doi:10.1007/s00382-011-1259-y.
- Watanabe, S., and Coauthors, 2011: MIROC-ESM: Model description and basic results of CMIP5-20c3m experiments. *Geosci Model Dev.*, **4**, 845–872, doi:10.5194/gmd-4-845-2011.
- Xin, X., W. Tong-Wen, and Z. Jie, 2013: Introduction of CMIP5 experiments carried out with the climate system models of Beijing Climate Center. *Adv. Climate Change Res.*, **4**, 41–49, doi:10.3724/SP.J.1248.2013.00041.
- Yukimoto, S., and Coauthors, 2012: A new global climate model of the Meteorological Research Institute: MRI-CGCM3—Model description and basic performance. *J. Meteor. Soc. Japan*, **90A**, 23–64, doi:10.2151/jmsj.2012-A02.